Holzforschung, Vol. 65, pp. 811–818, 2011 • Copyright © by Walter de Gruyter • Berlin • Boston. DOI 10.1515/HF.2011.110

Determination of local material properties of OSB sample by coupling advanced imaging techniques and morphology-based FEM simulation

Vaclav Sebera[1,*] and Lech Muszyński[2]

[1] Department of Wood Science, Faculty of Forestry and Wood Technology, Mendel University in Brno, Zemedelska 3, 613 00 Brno, Czech Republic

[2] Department of Wood Science and Engineering, College of Forestry, Oregon State University, 119 Richardson Hall, Corvallis, Oregon 97331, USA

*Corresponding author.
Department of Wood Science, Faculty of Forestry and Wood Technology, Mendel University in Brno, Zemedelska 3, 613 00 Brno, Czech Republic
Phone: +420 545 134 045
E-mail: vaclav.sebera@mendelu.cz

Abstract

The goal was to determine local mechanical properties inside of oriented strand board (OSB) based on a realistic morphology-based finite element (FE) model and data acquired from a physical test performed on the same material. The spatial information and local grayscale intensity from CT-scans obtained from small OSB sample was transformed into a 2D regular morphology-based FE mesh with corresponding material properties. The model was then used to simulate the actual compression test performed on the specimen using simplified boundary conditions. The simulated strain fields from the model were compared with the actual strain field measured on the specimen surface during the compression test by means of a full-field optical method, named digital image correlation (DIC). Finally, the original set of material properties was adjusted by an iterative procedure to minimize the difference between the simulated and the measured strain data. The results show that the developed procedure is useful to find local material properties as well as for morphological modeling without the need of segmentation of the image data. The achieved results serve as a prerequisite for full 3D analyses of the complex materials.

Keywords: digital image correlation; finite element method; inverse problem methodology; morphological modeling; OSB.

Introduction and literature review

The prediction and evaluation of the behavior of complex heterogeneous materials (e.g., bones, composites, wood) is still a serious challenge in many research fields. One of the most effective approaches is to use numerical modeling, where the problem is approximated by discretization of the material geometry (finite element method (FEM), material point method (MPM), lattice models etc.) and application of simplified boundary conditions. The usefulness of such models is, however, limited by the quality of the local material characteristics in the elements. As reliable local properties are difficult to obtain and not easy to incorporate in a model, a common practice is to apply homogenized material properties across the larger material types. This however, may not be sufficient for materials, which, like wood particles in wood-based composites, are characterized by wide ranges of mechanical properties. Another difficulty is an adequate representation of the material internal structure. There are two main approaches to obtain the representative material structure (Muszyński and Launey 2010).

In the first approach, the somewhat idealized internal structure of the material is generated by the researcher based on the general knowledge of its morphological characteristics. These characteristics can be specified deterministically or randomized to a certain degree to fulfill the statistical and spatial variability of them within the material. Hence, usually a set of objects (elements) is obtained, which may be unique but which exhibit a similar pattern or periodic structure resulting from the underlying assumptions and the empirical data on which they are based.

In the second approach, the realistic structure or morphology of the material sample is generated from 2D or 3D digital images of the material specimen. The images may be obtained by various imaging techniques including computed tomography (CT), scanning electron microscopy (SEM), nuclear magnetic resonance (NMR), and many others (Bucur 2003; Kherlopian et al. 2008; Muszyński 2009). This method does not require an idealization of the internal structure of the material nor a priori knowledge of its characteristics and is often called morphological- or anatomy-based modeling. However, in order to be accurate, the method requires that the image of the sample is statistically representative for the material. Problems may arise when the images are difficult to interpret in the raw state in which they were acquired. For these reasons, image processing procedures (for instance noise reduction, image segmentation, etc.) are often needed before the images can be used as input data in further modeling processes. Segmentation is the subdivision of the image into its constituent regions or objects according to a selected level of detail and is one of the most difficult tasks in image processing (Gonzales et al. 2004; Bache-Wiig and Henden 2005). This operation is crucial because the regions (lines, areas, volumes) may be the objects needed for transformation into a computational model. Therefore, the accuracy of morphology-based approach is also dependent upon the tech-

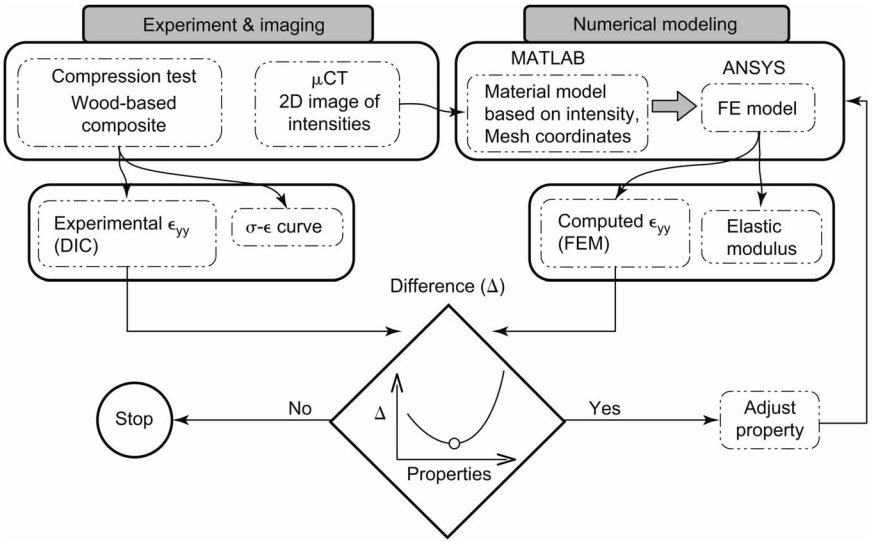

Figure 1 Work and data flow – inverse problem methodology (based on Lecompte et al. 2005).

niques of image acquisition, image processing, and the degree of discretization of the segmented data.

Although the first approach is more common, both are well established and used efficiently for modeling a sizeable range of complex materials, such as wood and wood based composites (WBC), but also of other biomaterials, e.g., bones (Haitao et al. 2009; Lüpke et al. 2010), polycrystalline materials (Ludwig et al. 2009), and carbon fiber composites (Feraboli et al. 2010). A review by Mackerle (2005) summarizes the first approach described in more than 260 papers concerning the application of FEM in wood science between 1995 and 2004. Specifically, the first (FEM) approach is useful at the level of the cell wall or assemblies of cells (Holmberg et al. 1999; Javořík 2000, 2002) and at the level of cells and tree rings with a probabilistic methodology (Koňas 2003). It was also applied on wood strands with distinguished tree rings (Hindman and Lee 2007). A randomized structure for creating and analyzing the WBC was the method of choice in publications of Faessel et al. (2005) or Dai (2007) and Li et al. (2009), in which the Monte Carlo methods were used. Problems of fracture mechanics solved by this approach are reviewed in Smith et al. (2007) and more recently showed in de Moura et al. (2009) and Dourado et al. (2010).

The second approach is particularly suitable for MPM modeling, because of the ease of converting the digital images into material point mesh (Nairn 2006, 2007) although FEM is also very common (Badel and Perré 2002, 2003; Perre 2005; Koňas et al. 2009). While reconstruction of the images is not problematic for fibrous materials like fiberboard (Faessel et al. 2005; Badel et al. 2008), paper (Axelsson and Svensson 2010), or wood itself (Trtik et al. 2007), it is a challenge for materials like orientated stand board (OSB) (Muszyński 2009).

Both approaches are able to predict the mechanical behavior of materials or their structural elements or assemblies with certain assumptions regarding the local material properties. In both methods, the material properties are either assumed to be uniform, in this case the source of the heterogeneity of the material is its morphological structure, or properties are specifically assigned to groups of elements (material points based on the a priori knowledge of their distribution).

One way to overcome this difficulty is the inverse problem method (IPM). This method takes advantage of recent progress in full field measurement techniques, e.g., digital image correlation (DIC) (Pan et al. 2009; Sutton 2008), which return displacement and strain data equivalent to thousands of strain gages. Thus, local deformation gradients and strain concentrations can be captured, either in 2D or 3D (Forsberg et al. 2008). Their output format is compatible with numerical modeling packages based on FEM or MPM, so the measured and simulated displacement and strain fields can be directly compared. This comparison is helpful to find local material properties of heterogeneous and complex materials (Grediac and Pierron 1998; Pierron and Grediac 2000; Muszyński and Launey 2010). The conceptualization of this method together with the procedure of our work is shown on the diagram in Figure 1.

The general goal of this study was to develop a procedure for using a morphology-based FE model of an OSB sample and the data acquired from a physical test performed on the same material to determine the local mechanical properties of the sample with the assistance of the simplified IPM. The study was performed in four stages: 1) translation of the spatial information and local grayscale intensity from CT-scan of a small OSB sample into regular morphology-based FE mesh with corresponding material properties; 2) FE simulation of the actual nondestructive compression test performed on the specimen after scanning, relying on the actual boundary conditions; 3) comparison of the simulated strain fields from the FE model with the actual strain field measured on the specimen surface during actual compression test; 4) use an iterative procedure to adjust the original set

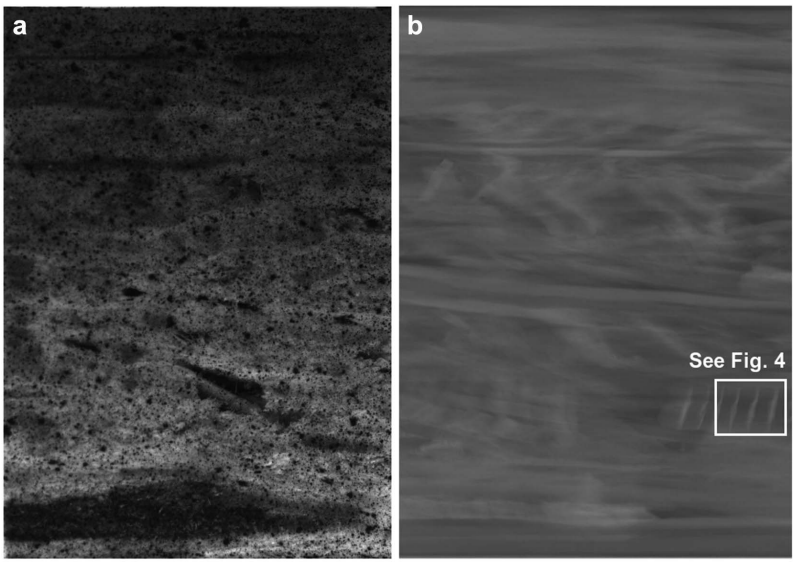

Figure 2 (a) A digital photograph of the WBC side surface, (b) a 2D X-ray image reflecting 3D material organization of the WBC specimen.

of material properties in a way that the difference between the simulated and measured strain is minimized. This work is expected to provide a platform for the development of novel modeling methods that avoid segmentation, yet preserve material morphology.

Material and methods

The study was divided into two phases: the experimental phase, in which the sample was scanned by X-CT and physically tested and the virtual phase, which included numerical modeling and data analysis.

For the experimental measurements, a specimen of $12.5 \times 12.5 \times 18$ mm^3 was cut through the entire thickness of an OSB board (Figure 2a). The procedure and work flow (Figure 1) can be divided into four main steps: 1) X-CT scanning of the OSB sample; 2) optical measurement of the deformations on the sample in a non-destructive compression test to provide full-field strain data; 3) numerical modeling – building the FE mesh based on the X-CT data of the OSB sample and simulating the physical test in the FE model; 4) iterative procedure for the determination of local material properties by comparing the simulated and the measured results.

Generation of the X-CT scan

The specimen was scanned in an X-ray CT scanner [Scanco Medical (Basserdorf, Switzerland) μCT 40 with 12 μm/voxel resolution] and 3D X-ray attenuation data set was obtained. The X-ray attenuation coefficient (μ) of each voxel in this volume is represented by an 8 bit grayscale intensity (0 for black and 255 for white, Figure 2b). The volumetric intensity data were projected onto the front side of the specimen resulting in a 2D image equivalent to single X-ray radiogram of the sample. The full 3D data will be used in a later stage of the study.

Compression test and optical measurement

After scanning, the specimen was subjected to a compression test performed on a small scale universal testing machine (Instron 5500 series EM, Norwood, MA, USA) following a slightly modified ASTM D3501 – 05a. The full-field displacement and strain maps across the thickness were measured on the side of the specimen by means of an optical measurement system based on the DIC principle (Vic-3D by Corelated Solutions Inc., Columbia, SC, USA). The DIC measurement provided a matrix of strain in the Y-axis direction (ε_{yy}) with a resolution of 231×411 points. This test also provided a homogenized (average) elastic modulus (E_m) for the sample that was computed from the linear part of the stress-strain curve. This value was used as a base in the next steps of work.

Numerical modeling

Generally, a numerical simulation of a compression test requires the following input information: a) spatial data of elements – FE mesh, b) a constitutive model and related material properties of the FEs derived from X-CT data, and c) boundary conditions reflecting the actual compression test.

Generating FE mesh from CT data

The FE mesh is based on the digital image produced by projecting the volumetric X-CT data on the front side of the specimen. The image was converted into a regular FE grid of squares that corresponded to the grid of 4×4 pixels in the projected image, effectively reducing the resolution from 1024×1784 pixels to 256×446 pixels. The resulting scaling factor f was $f = 22.36$ pixels per 1 mm. After that, 3 top pixel rows were removed from the mesh in order to eliminate pixels of air above the specimen. Pixel coordinates and material properties derived from pixel intensities were then exported to FEM software (ANSYS v. 11, ANSYS Inc., Canonsburg, PA, USA) to serve as spatial information for FE mesh. A detailed description of the method for deriving material properties is provided below. This regular FE mesh consisted of 113,408 linear PLANE42 finite elements with 2 degrees of freedom (DOFs). PLANE42 finite element was chosen because it supports the definition of the multi-elastic material option (MEM) described in some detail below. The resulting problem consisted of approximately 228,000 equations to be solved per iteration. A detail of the image from Figure 2b and the corresponding FE mesh is shown in Figure 3. It is clear that the

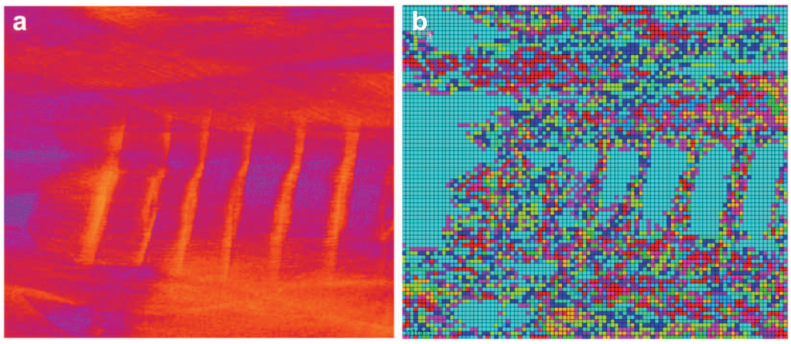

Figure 3 (a) A detail of CT image of the WBC specimen from Figure 2b in full resolution as acquired by X-ray (to enhance detail a different color map is used), (b) the corresponding FE model in reduced (computing) resolution with material models distinguished in color (ANSYS).

morphology of the material is preserved, although with reduced resolution.

Deriving element properties from CT data

Before the material properties from the X-CT scan were derived, three simplifying assumptions were made. First, a linear correlation between intensity (I) and density was assumed based on an experimentally derived linear relationship between the X-ray attenuation coefficient and density of wood (Lindgren 1985). Consequently, the pixel intensities are linearly mapped on local densities in the specimen. Second, a linear correlation was supposed between the density and the elastic modulus (MOE) of wood in the transverse direction (the direction of loading). This relationship was experimentally determined by Holz (1974, 1981), Vavrčík et al. (2008) and Forest Product Laboratory (2010). These two assumptions resulted in a linear correlation between the intensity and the MOE. Finally, the third assumption was that the behavior of an OSB sample under compression perpendicular to the grain could be safely simplified as being isotropic. Note that in OSB the strands are already somewhat densified during pressing in order to achieve desired compaction ratio. Poisson ratio was supposed to be 0.3.

The image in Figure 2b was the basis for deriving the elastic modulus (E_i) distribution from local pixel intensities. The histogram of grayscale intensities of all pixels in the image is shown in Figure 4a. By virtue of the assumed correlation between the intensities and elastic modulus, this histogram represents both the distribution of the intensity (X-ray attenuation) within the OSB sample and the distribution of the elastic modulus for the FE model. The measured modulus of the bulk sample E_m was identified with the mean value in the histogram, and the local elastic moduli for FE model were derived from the following linear function:

$$E_i = E_m + b_i(I_{kl} + I_m), \tag{1}$$

where E_i is the matrix of local elastic moduli for the FE model, $i = (1, 10)$, E_m is a scalar representing the mean value of E for the bulk composite given by experimental measurement, b_i is the scalar representing the slope of the linear function, I_{kl} is the matrix of pixel intensities (image) with k rows and l columns, I_m is a scalar which represents the mean intensity of the image ($I_m = 117$).

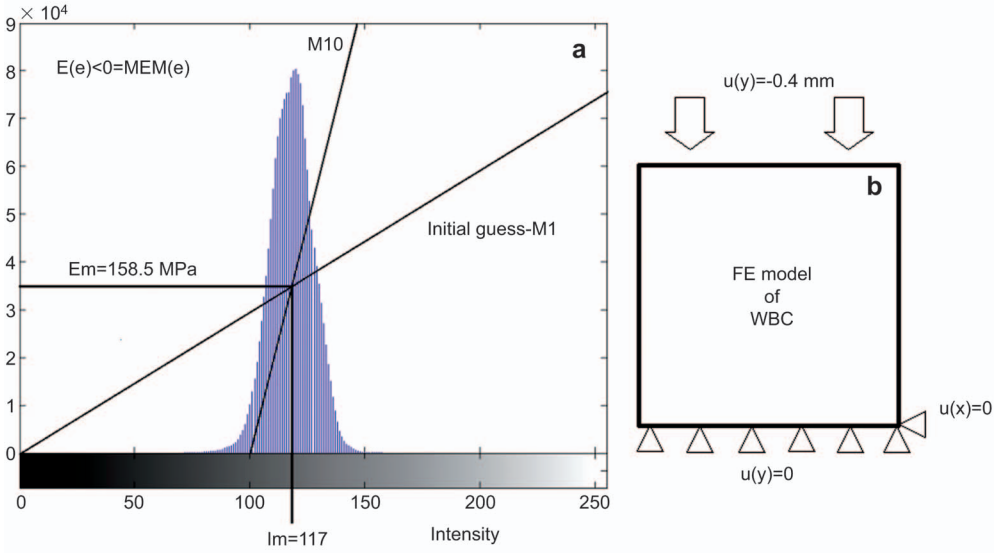

Figure 4 (a) The histogram of the image in Figure 2b with sketch of the procedure of deriving particular FE models, (b) boundary conditions of FE models where u(x) and u(y) mean a node displacement in X- and Y-axis directions.

Table 1 Overview of material models used in finite element (FE) simulations and computed elastic moduli.

	Elastic moduli for particular FE models (MPa)									
	M1	M2	M3	M4	M5	M6	M7	M8	M9	M10
Min	108.7	103.2	96.3	87.4	75.5	58.9	34.1	1.5	MEM	MEM
Max	205.4	210.6	217.1	225.4	236.6	252.2	275.7	314.7	392.8	627.1
Mean	158.5	158.5	158.5	158.5	158.5	158.5	158.5	158.5	158.7	164.0
# of elements with MEM	0	0	0	0	0	0	0	0	360 (0.32%)	9955 (8.78%)
Computed by FE simulation	143.2	143.1	142.9	142.7	142.3	141.6	140.3	137.0	123.5	60.6

Boundary conditions

In Figure 4b the boundary conditions are shown. All the bottom nodes of the FE model are constrained in the Y direction; however, the bottom-right node is also constrained in the X direction in order to avoid rigid body motion of the model. A displacement of 9.016 px (0.4 mm) was applied to the top nodes to simulate a compression performed on the Instron 5500.

Inverse problem methodology

In order to obtain a set of local elastic moduli for the inverse problem method algorithm, it was necessary to define a global variable for the iterations. Because of the assumed linear correlation between E and I, the most convenient choice was the slope of the linear function in Equation 1. In the course of the procedure, the variable was increased in 10 finite increments, resulting in 10 different material property sets for FE models (M1–M10). All those sets went into simulations. A schematic representation of this procedure can be seen in Figure 4a, where FE model 1 (M1) represents the initial set of the material properties (E_1) and model 10 (M10) represents the final set (E_{10}). In order to avoid computational problems in the FE analyses, the elements with numerically possible ''negative elastic moduli'' were considered voids and were modeled with an MEM model. MEM is a multi-linear function available in ANSYS defined through section-wise strain/stress ratios (ε/σ), which are activated depending on the strain level in the element. In this project, the ε/σ values in MEMs representing voids were: 0/0, 0.3/0.3, 0.8/79 and 1/79. PLANE42 finite element was chosen because it supports the definition of the MEM. In Table 1, the range of MOE for each iteration and corresponding void contents are presented.

Once all simulations were completed, they were compared with the DIC results. First, the standard error based on the measured and simulated values was calculated as follows:

$$St_{error} = \sqrt{\frac{1}{m \cdot n} \sum_{i=1}^{m \cdot n} (DIC_i - FEM_i)^2}, \quad (2)$$

where DIC_i is the εyy of i-element measured by DIC [-], FEM_i is the εyy of i-element computed in ANSYS [-], $m.n$ is the number of elements to be compared. Equation 2 is similar to an expression of the standard deviation, but its computation is not related to the mean value of the set. Instead, it is performed element-wise and represents the standard error of one matrix compared to the other. Standard error values and homogenized elastic moduli for the entire sample were calculated for all 10 iterations. The homogenized modulus was computed from reaction forces (RF) at constrained nodes in both the X-axis and Y-axis directions as:

$$E = \frac{RF \cdot d}{d \cdot w \cdot \varepsilon \cdot f}, \quad (3)$$

where E is the mean modulus of the sample [MPa], RF is the 2D reaction forces [Npx^{-1}], f is the scaling factor ($f = 22.36$ pixels mm^{-1}), d is the depth of the specimen [mm], w is the width of the specimen [mm] and ε is the strain [-]. The computed E was further compared to the elastic modulus given by experimental measurement – E_m. A visual comparison of the measured and simulated vertical strain maps on the surface of the specimen was also performed.

Results and discussion

The compression test

The results obtained from the optical measurements (DIC) during the compression test are shown in a vertical strain component map in Figure 5a. The strain field is based on nearly 95,000 reference points arranged in a 231×441 grid, reflecting the complicated inner structure of the composite, i.e., regions with higher and lower density of material (stiffness). Although the strain field is highly non-uniform within the material, the bottom and top thirds exhibit a more uniform strain than the middle section. It is important to note that the strain field depicted here is on the surface of the specimen and does not represent the strain state throughout its 3D volume. The average elastic modulus (Em) of the sample was computed from the linear part of nominal stress vs. the average strain curve. Em is 158.5 MPa.

Numerical simulation

Figure 5b,c depicts strain fields computed from two iterations of FE simulations – M8 and M10. These strain fields visibly differ from the strain field obtained from optical measurement. One reason is that the strain field from FE simulation is based on a virtual radiograph reflecting mean intensities of the 3D volume of the composite in 2D, while the DIC strain field is computed on the surface and may differ significantly throughout the material's thickness. This means that ε_{yy} from the FE simulation reflects the 3D structure (morphology) of the specimen even though it was projected into a 2D plane. Despite the implicit differences, certain regions of interest are arranged in a similar pattern on both FE and DIC images (marked with polygon frames in Figure 5). These regions represent places where the internal features of the composite's organization are large enough to influence the strain on the surface of the specimen (Figure 5a). While the strain fields of the FEM and DIC are within the same range for M8, the ranges diverge for M10, causing a higher error of computation accordingly. Generally, the

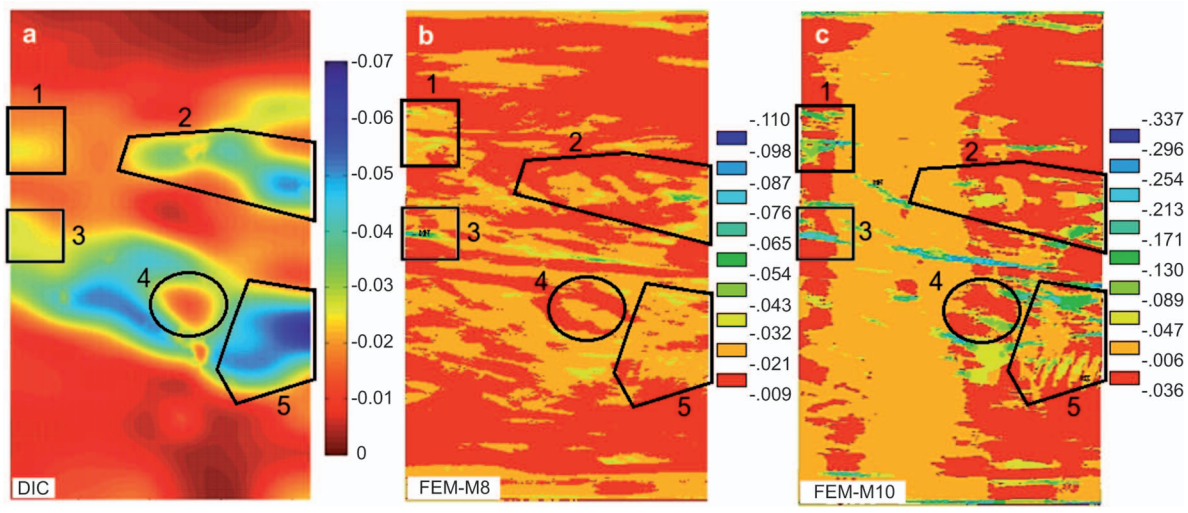

Figure 5 Graphical results (a) εyy on OSB surface from the DIC measurement, (b) εyy from M8 FE simulation, (c) εyy from M10 FE simulation. Significant areas of interest from DIC measurement are framed and then copied to corresponding areas from FE analyses results.

strain maps obtained from simulations (M1–M9) can be divided into three regions where the central one exhibits significantly higher strain than the others. This aspect of the output is similar to the measured results.

The standard error was calculated for consecutive iterations 1 to 10 by Equation 3 to assess the difference between the simulated and measured strain fields (Figure 6a). The standard error between M1 and M8 decreases very slowly, except for the second iteration (M2) where exceptionally high error occurs. An increasing number of voids (MEMs) causes the standard error to increase abruptly with iteration M9. M10 contains more voids (ca. 9%) than real material samples (Zombori et al. 2001), and thus it represents a hypothetical scenario of OSB material organization (Figure 6b). This abundance of voids drives the dramatic increase in standard error. The minimum standard error is achieved at iteration M8, indicating the best set of local material properties with respect to DIC measurement. This is achieved for $b_8 = 4.474$ (Equation 1) connoting the point at which the material properties are optimized in the 10-iteration procedure.

The comparison of the homogenized elastic moduli calculated from the simulated reaction forces is summarized in Table 1. The homogenized modulus E decreases very gradually from 143 to 140 MPa for the first 7 iterations (M1–M7), and then decreases rapidly from 137 to 60.6 MPa in the last 3 iterations (M8–M10). This occurs because more elements are classified as voids which do not contribute to the stiffness of the sample within each iteration. It is important to note that the magnitude of this effect depends on the material organization or the location of voids in the material. For instance, the total void content in iteration M10 was ca. 9%, but the homogenized modulus E was about 56% lower

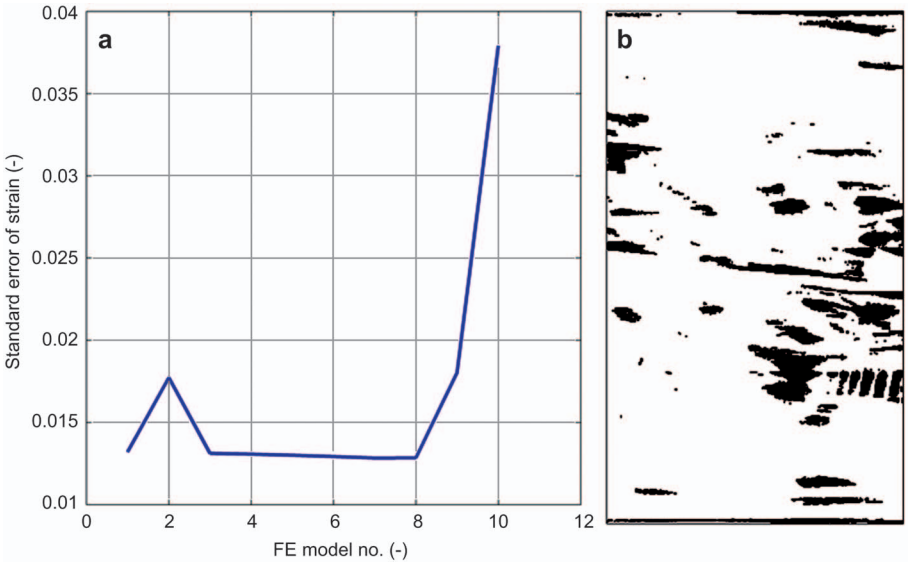

Figure 6 Standard error of FEM strain field in comparison to DIC measurement, (b) content of voids (dark areas, ca. 9%) in the FE model (M10 variant) of the WBC specimen.

than that calculated in iteration M8, the last simulation without MEM-voids. The difference between the *E* given by the M8 simulation and the value measured experimentally by Instron 5500 is ca. 21.5 MPa. Perfect agreement would be achieved if all finite elements had the same elastic moduli; this would be the case if the linear function in Figure 4 was a horizontal line (a constant) and the strain field would be uniform as in a homogeneous material.

Some of the differences between experimental and numerical results may be partly attributed to the simplifying assumptions (i.e., the linear correlation between X-ray attenuation and the elastic modulus, and isotropic response of the composite to the transverse load). Resolving the orthotropic properties of each strand included in the sample would require identification of the orientation of individual strands in 3D and 3D simulation of the actual test. Characterizing strand orientation from CT data is a challenging task outside the scope of this study, in which we sought for developing the inverse problem procedure for identification of local material properties. Here, the voids were modeled as FEs with the help of MEM to avoid considering the contact around the void when collapse would occur. The sheer quantity of contact pairs, such as in the cases of M9 and M10, exhibiting highly nonlinear behavior could generally lead to a divergent solution. Hence, MEM was utilized to integrate attributes of the FE ''birth and death'' technique that is common in the field of numerical simulations.

The accuracy of our model depends on the resolution of X-CT scan data as the FE model is derived from the image. Higher resolution images provide more material morphology data that may improve the FE models to a certain degree, however, the consequent increase of DOFs produces additional equations to be solved. If the same simulation was considered in 3D for a $256\times446\times256$ voxel image with 3 DOFs per node, the problem would increase from 228 thousand equations in 2D to approximately 87 million equations. FE analysis of such a size is still considered as a problem due to computational limitations (parallelization and clusters must be used). It is noteworthy, that mesh density in FE models seems to have negligible impact on the computed homogenized elastic modulus. After meshing each pixel area by 4 FEs, the E_m value was the same for all iterations. This result agreed with the findings of Feraboli et al. (2010) among others, where authors investigated the influence of 3 different mesh densities on calculation of strain in particular areas. Those areas did not correspond to the pixels (as in our case), but to randomly produced representative volume elements.

Conclusions

Here, a procedure that combines a morphology-based FE model of a heterogeneous sample and the data acquired from a physical test performed on the same material, to determine the local mechanical properties of the sample with the assistance of the simplified inverse problem method, has been developed. The utility of this approach was demonstrated on data recorded from an OSB sample. The best match between the strain fields generated from FE simulations and optical measurement (DIC) of surface strains was optimized through 10 iterations of the procedure. The quality of the match, measured as the standard error between the measured and simulated strain field for each point of measurement was best for iteration M8. Although visual inspection of the strain maps reveals obvious differences, some common significant features were recognized. The homogenized elastic modulus for bulk composite deviated somewhat from the measured modulus used as the initial guess for the simulation procedure at iteration M8.

The study has shown that morphology-based modeling of complex materials can be performed with reasonable accuracy without rigorous image segmentation. It offers a relatively easy way to model complex heterogeneous materials like OSB and other bio-based composites. In future work, we hope to extend the 2D FE model of the composite to 3D and consider strand orientation in order to determine full orthotropic material properties.

Acknowledgements

The authors are much obliged to the J.W. Fulbright commission for supporting the project ''Wood and wood-based composites – materials for sustainable future. Numerical modeling and optimization''. The authors are also grateful to Dr. Urszula Iwaniec from the Skeletal Biology Laboratory at OSU for the assistance with scanning the OSB sample.

References

ASTM Standard (2005) D3501 – 05a. Standard Test Methods for Wood-Based Structural Panels in Compression. American Society for Testing and Materials.

Axelsson, M., Svensson, S. (2010) 3D pore structure characterization of paper. Pattern Anal. Appl. 13:159–172.

Bache-Wiig, J., Henden, P. Ch. (2005) Individual fiber segmentation of three-dimensional microtomograms of paper and fiber-reinforced composite materials. Master thesis. Paper and Fiber Research Institute, Norway.

Badel, É., Perré, P. (2002) Predicting oak wood properties using X-ray inspection: representation, homogenisation and localisation. Part I: digital X-ray imaging and representation by finite elements. Ann. For. Sci. 59:767–776.

Badel, É., Perré, P. (2003) Predicting of oak wood properties using X-ray inspection: representation, homogenisation and localisation. Part II: computation of macroscopic properties and microscopic stress fields. Ann. For. Sci. 60:247–257.

Badel, É., Delisee, C., Lux, J. (2008) 3D structural characterisation, deformation measurements and assessment of low-density wood fiberboard under compression: the use of X-ray microtomography. Compos. Sci. Technol. 68:1654–1663.

Bucur, V. (2003) Nondestructive Characterization and Imaging of Wood. Springer-Verlag, Berlin.

Dai, Ch. (2007) Modeling formation and bonding of wood composites. Presentation presented at FPInnovation – Forintek Division, Vancouver, Canada.

de Moura, M.F.S.F., Silva, M.A.L., Morais, J.J.L., de Morais, A.B., Lousada, J.J.L. (2009) Data reduction scheme for measuring G_{IIc} of wood in end-notched flexure (ENF) tests. Holzforschung 63:99–106.

Dourado, N.M.M., de Moura, M.F.S.F., Morais, J.J.L., Silva, M.A.L. (2010) Estimate of resistance-curve in wood through the double cantilever beam test. Holzforschung 64:119–126.

Faessel, M., Delisee, C., Bos, F., Castera, P. (2005) 3D Modelling of random cellulosic fibrous networks based on X-ray tomography and image analysis. Compos. Sci. Technol. 65:1931–1940.

Feraboli, P., Clevelend, T., Stickler, P., Halpin, J. (2010) Stochastic laminate analogy for simulating the variability in modulus of discontinuous composite materials. Compos. Pt. A-Appl. Sci. Manuf. 41:557–570.

Forest Product Laboratory (2010) Wood handbook – Wood as an engineering material. General Technical Report FPL-GTR-190. U.S.D.A., Forest Products Laboratory, Madison.

Forsberg, F., Mooser, R., Arnold, M., Hack, E., Wyss, P. (2008) 3D micro-scale deformations of wood in bending: synchrotron radiation μCT data analyzed with digital volume correlation. J. Struct. Biol. 164:255–262.

Gonzales, R.C., Woods R.E., Eddins, S.L. (2004) Digital Image processing Using Matlab. Pearson Prentice Hall.

Grediac, M., Pierron, F. (1998) A T-shaped specimen for the direct characterization of orthotropic materials. Int. J. Numer. Methods Eng. 41:293–309.

Haitao, X., Yulong, L., Lingcheng, Z., Weiguo, G. (2009) Nonlinear finite element analysis of the vibration characteristics of the maxillary central incisor related to periodontal attachment. Med. Biol. Eng. Comput. 47:1189–1195.

Hindman, P.D., Lee, N.J. (2007) Modeling wood strands as multilayer composites: bending and tension loads. Wood Fiber Sci. 39:515–526.

Holmberg, S., Persson, K., Petterson, H. (1999) Nonlinear mechanical behaviour and analysis of wood and fibre materials. Comput. Struct. 72:459–480.

Holz, D. (1974) On some important properties of non-modified coniferous and broad leaved woods in view of mechanical and acoustical data in piano soundboards. Arch. Akustyki. 9:37–57.

Holz, D. (1981) Zum Alterungsverhalten des Werkstoffes Holz – einige Ansichten, Untersuchungen, Ergebnisse. Holztechnologie 22:80–85.

Javořík, J. (2000) Numerical simulation of mechanical behavior of wood on microscopic level. MendelNet conference. MU in Brno. p. 43. [in Czech]

Javořík, J. (2002) A numerical model of microstructure of the wood and a structural analysis of the wood. MendelNet conference. MU in Brno. pp. 117–124. [in Czech]

Kherlopian, R.A., Song, T., Duan, Q., Neimark, M.A., Po, M.J., Gohagan, J.K., Laine, A.F. (2008) A review of imaging techniques for systems biology. BMC Syst. Biol. 2:74.

Koňas, P. (2003) General concept of finite element (FE) model based on anatomy structure (Part V – probabilistic FEM model of wood). Acta Univ. Agric. et Silvic. Mendel. Brun. 1:69–79.

Koňas, P., Gryc, V., Vavrčík, H. (2009) 3D visualization and finite element mesh formation from wood anatomy samples, Part I – Theoretical approach. Acta Univ. Agric. et Silvic. Mendel. Brun. 1:1–16.

Lecompte, D., Sol, H., Vantomme, J., Habraken, A.M. (2005) Identification of Elastic Orthotropic Material Parameters Based on ESPI Measurements. SEM Annual Conference & Exposition on Experimental and Applied Mechanics. Portland, USA, 1–7.

Li, P., Dai, Ch., Wang, S. (2009) A simulation of void variation in wood-strand composites during consolidation. Holzforschung 63:357–361.

Lindgren, L.O. (1985) On the relationship between density/moisture content in wood and X-ray attenuation in computer tomography. Proceedings 5th Symposium Nondestructive testing of wood; Washington state university, Eng. Publishing, Pullman, pp 193–203.

Ludwig, W., King, A., Reischig, P., Herbig, M., Lauridsen, E.M., Schmidt, S., Proudhon, H., Forest, S., Cloetens, P., Rolland du Roscoat, S., Buffière, J.Y., Marrow, T.J., Poulsen, H.F. (2009) New opportunities for 3D materials science of polycrystalline materials at the micrometre lengthscale by combined use of X-ray diffraction and X-ray imaging. Mat. Sci. Eng. A-Struct. 24:69–76.

Lüpke, M., Gardemin, M., Kopke, S., Seifert, H., Staczyk, C. (2010) Finite element analysis of the equine periodontal ligament under masticatory loading. Wien. Tierarz. Monats. 97:101–106.

Mackerle (2005) Finite element analyses in wood research: a bibliography. Wood Sci. Technol. 39:579–600.

Muszyński, L. (2009) Is what you see all you can get? Bridging experimentation and modelling with advanced imaging techniques. In proceedings of the Final Conference of COST Action E49: processes and Performance of Wood-based Panels, Nantes, France, September 14–15, (Ed. M. Irle): 71–83.

Muszyński L., Launey, M.E. (2010) Advanced imaging techniques in wood-based panels research. In: Wood-Based Panels – An Introduction for Specialists. State-of-the-Art in Wood-Based Panels Research. COST Action E49:177–201.

Nairn, J. (2006) Numerical Simulations of Transverse Compression and Densification in Wood. Wood Fiber Sci. 38:576–591.

Nairn, J.A. (2007) Material point method simulations of transverse fracture in wood with realistic morphologies. Holzforschung 61:375–381.

Pan, B., Qian, K., Xie, H., Asundi, A. (2009) Two-dimensional digital image correlation for in-plane displacement and strain measurement: a review. Meas. Sci. Technol. 20:1–17.

Perre, P. (2005) Meshpore: a software able to apply image-based meshing techniques to anisotropic and heterogeneous porous media. Dry. Technol. 23:1993–2006.

Pierron, F., Grediac, M. (2000) Identification of the through-thickness moduli of thick composites from whole-field measurements using the Iosipescu fixture: theory and simulations. Compos. Pt. A-Appl. Sci. Manuf. 31:309–318.

Smith, I., Snow, M., Asiz, A., Vasic, S. (2007) Failure mechanisms in wood-based materials: a review of discrete, continuum, and hybrid finite-element representations. Holzforschung 61:352–359.

Sutton, M.A. (2008) Digital image correlation for shape and deformation measurements. In: Springer handbook of experimental solid mechanics. Ed. Sharpe, W.N. Springer-Verlag, Heidelberg. pp. 565–600.

Trtik, P., Dual, J., Keunecke, D., Mannes, D., Niemz, P., Stähli, P., Kaestner, A., Groso, A., Stampanoli, M. (2007) 3D imaging of microstructure of spruce wood. J. Struct. Biol. 159:46–55.

Vavrčík, H., Gryc, V., Rybníček, M. (2008) Variability of selected physical and mechanical properties of English oak wood. Influence of age, trunk radius and height. Lesnická práce, s.r.o., Kostelec nad Černými lesy. [in Czech]

Zombori, B.G., Kamke, F.A., Watson, L.T. (2001) Simulation of the mat formation process. Wood Fiber Sci. 33:564–579.

Received December 17, 2010. Accepted May 1, 2011.
Previously published online July 5, 2011.